RSC Advances

PAPER

View Article Online
View Journal | View Issue

Cite this: *RSC Adv.*, 2022, **12**, 907

Novel mesoporous Co_3O_4–Sb_2O_3–SnO_2 active material in high-performance capacitive deionization

Ehsan Delfani,[a] Alireza Khodabakhshi,[a] Sajjad Habibzadeh,*[a] Leila Naji[b] and Mohammad Reza Ganjali[c]

Capacitive deionization (CDI), as an emerging eco-friendly electrochemical brackish water deionization technology, has widely benefited from carbon/metal oxide composite electrodes. However, this technique still requires further development of the electrode materials to tackle the ion removal capacity/rate issues. In the present work, we introduce a novel active carbon (AC)/Co_3O_4–Sb_2O_3–SnO_2 active material for hybrid electrode capacitive deionization (HECDI) systems. The structure and morphology of the developed electrodes were determined using X-ray diffraction (XRD), X-ray photoelectron spectroscopy (XPS), scanning electron microscopy (SEM), energy-dispersive X-ray spectroscopy (EDS), and Brunauer–Emmett–Teller (BET)/Barrett–Joyner–Halenda (BJH) techniques, as well as Fourier-transform infrared (FT-IR) spectroscopy. The electrochemical properties were also investigated by cyclic voltammetry (CV) and impedance spectroscopy (EIS). The CDI active materials AC/Co_3O_4 and AC/Co_3O_4–Sb_2O_3–SnO_2 showed a high specific capacity of 96 and 124 F g^{-1} at the scan rate of 10 mV s^{-1}, respectively. In addition, the newly-developed electrode AC/Co_3O_4–Sb_2O_3–SnO_2 showed high capacity retention of 97.2% after 2000 cycles at 100 mV s^{-1}. Moreover, the electrode displayed excellent CDI performance with an ion removal capacity of 52 mg g^{-1} at the applied voltage of 1.6 V and in a solution of potable water with initial electrical conductivity of 950 μs cm^{-1}. The electrode displayed a high ion removal rate of 7.1 mg g^{-1} min^{-1} with an excellent desalination–regeneration capability while retaining about 99.5% of its ion removal capacity even after 100 CDI cycles.

Received 12th October 2021
Accepted 20th December 2021

DOI: 10.1039/d1ra07557h

rsc.li/rsc-advances

1. Introduction

The shortage of potable water has lately turned into an inevitable challenge. Therefore, freshwater production from brackish water (salinity < 5 g L^{-1})[1] through the desalination process has been looked upon as a promising resolution to address the water crisis.[2,3] Several desalination technologies have been applied to remove dissolved solids in water.[3] Namely, the large-scale desalination techniques for greater salt concentration encompass reverse osmosis (RO) and thermal separation systems. Such techniques which eliminate the major phase (*i.e.*, water) from the solution suffer from high energy consumption and complex operation.[4,5] However, water with lower salt concentration, *e.g.*, brackish water, can be effectively desalinated with various newly developed techniques. Specifically, capacitive deionization (CDI) has been recognized as an eco-friendly electrochemical desalination technology for removing ionic species from aqueous solutions, which has been engaged to desalinate brackish water and seawater.[6–8]

In CDI technology, influent saltwater passes through two high capacitive porous electrodes with a separator in between. Such porous electrodes are charged with an applied voltage lower than 2 V. As a result, cations and anions are electrostatically adsorbed onto an electrical double layer of porous carbon electrodes, which resembles the principles of the electrical double-layer capacitors.[7,9,10] Therefore, similar to the capacitors, the electrode materials should benefit from extensive ion accessibility, high specific surface area and electronic conductivity, fast ion mobility within the pore network, robust electrochemical stability, good wettability, low contact resistance between the electrode and the current collector, and more importantly low-cost active components.[11,12]

Thus far, numerous structures of carbon-based electrode materials, including activated carbon (AC), ordered mesoporous carbons (OMCs), carbon nanofibers (CNFs), carbon nanotubes (CNTs), carbon aerogel (CA), and graphene, have been investigated.[10,13–15] However, the carbon-based supercapacitors are restricted by their ion adsorption capacity per

[a]*Surface Reaction and Advanced Energy Materials Laboratory, Department of Chemical Engineering, Amirkabir University of Technology (Tehran Polytechnic), P.O. Box 15875-4413, Tehran, Iran. E-mail: sajjad.habibzadeh@mail.mcgill.ca*

[b]*Department of Chemistry, Amirkabir University of Technology (Tehran Polytechnic), P.O. Box 15875-4413, Tehran, Iran*

[c]*Center of Excellence in Electrochemistry, School of Chemistry, College of Science, University of Tehran, P.O. Box 11155-4563, Tehran, Iran*

available surface area.[16,17] Moreover, these carbon materials cannot fully exploit the available capacitance in lower electrolyte concentrations due to ions' limited access through the porous structure.[18] Therefore, hybrid electrodes, *i.e.*, carbon composites such as carbon/carbon, carbon/polymer, carbon/metal oxide, and carbon/polymer/metal oxide composites, have widely been employed in high-performance CDI systems. This is due to its moderate pore size distribution and high specific surface area.[11,19] Besides, hybrid electrode capacitive deionization (HECDI) combines adsorption mechanisms of non-faradaic and faradaic reactions. The former is based on the formation of electric double-layer capacitors, while the latter relies on the redox process occurring on the surface of the carbon/metal oxides electrodes.[20] Besides, the carbon/metal oxide composites reveal enhanced desalination performance compared with pristine carbon materials. This is mostly due to the increase of ion removal capacity, improvement in wettability, selective adsorption of ionic species affecting the targeted ion adsorption, or modification of the surface charge of the carbon electrodes, which enhance the charge efficiency.[11,12,20] Several metal oxides, including Co_3O_4,[21] TiO_2,[22–24] Fe_3O_4,[25] Fe_2O_3,[24] MnO_2,[26] ZnO,[21] ZrO_2,[27] CeO_2,[24] and SnO_2 (ref. 28) have so far been used in various CDI systems and supercapacitor's applications. Cai and coworkers have reported $NiCo_2S_4$ nanotube arrays on Ni foam for supercapacitors, which displayed a specific capacity of 15.58 F cm^{-2} at 10 mA cm^{-2}, and low capacity retention of 79.3% after 2000 cycles at 8 mA cm^{-2}.[29] Particularly, Co_3O_4, as the low-cost transition metal oxide, has fascinated more attention due to its high theoretical capacity of 3560 F g^{-1}.[30] Wang *et al.* synthesized 3D self-supported Co_3O_4@$CoMoO_4$ core–shell nano-pine forest (NPF) for supercapacitor application, which showed the specific capacity of 1902 F g^{-1}.[31] Kandasamy *et al.* fabricated 2D Co_3O_4/graphene using a hydrothermal method, which presented a low specific capacity of 1.75 F cm^{-2} at 1 mA cm^{-2}.[32] However, Co_3O_4 suffers from poor electrical conductivity and cycling stability.[33]

Herein, we developed a composite electrode of AC and mixed metal oxides (MMO) for HCDI system. The Co_3O_4 and Co_3O_4–Sb_2O_3–SnO_2 nanopowders have been synthesized by the solution combustion method. As a result, constructing a composite of AC/Co_3O_4 with SnO_2 as a promising cycling stability agent and Sb_2O_3 as an electronic conductivity promoter seems to address the poor performance of the pure Co_3O_4.[34–36] In the present study, we developed a synergetic approach to preparing a novel HCDI electrode composed of AC/Co_3O_4–Sb_2O_3–SnO_2.

2. Experimental method

2.1. Chemicals and substrates

Activated carbon, polytetrafluoroethylene (PTFE), and dimethylformamide (DMF) were purchased from Sigma-Aldrich. In addition, cobalt(II) nitrate hexahydrate ($Co(NO_3)_2\cdot 6H_2O$), tin(II) chloride dihydrate ($SnCl_2\cdot 2H_2O$), antimony(III) chloride ($SbCl_3$), urea ($CO(NH_2)_2$), nitric acid (HNO_3), and all other chemicals were provided from Merck.

2.2. Synthesis of metal oxides

Mesoporous Co_3O_4 and Co_3O_4–Sb_2O_3–SnO_2 nanoparticles were prepared by solution combustion synthesis (SCS) method similar to the approach were explained in our previous works.[37,38] The growth mechanism of metal oxides preparation by SCS method is demonstrated in Fig. 1. The SCS method can be regarded into four steps; (1) formation of the combustion mixture, (2) formation of the gel, (3) combustion of the gel, and (4) formation of the powder. The pH increase by the urea decomposition (urea as the fuel) induces the metal hydroxides in the dried gel, which is subsequently transformed into metal oxides. This coincides with metal oxide nucleation.[39] After burning the dried gel, the metal oxides particles form large aggregates. The aggregation mechanism determines the growth of the formed nuclei since the combustion reaction generates a considerable amount of heat. However, the mesoporous structure of the metal oxide can be somehow controlled by releasing a large number of gases such as CO_2, N_2, and NO_x, *etc.* Hence, a trade-off of the generated heat and the gas evolution can shape the porous structure of the synthesized nanoparticles. In the synthesis process of Co_3O_4, ($CO(NH_2)_2$) and $Co(NO_3)_2\cdot 6H_2O$ were used as the fuel and oxidizer, respectively. The combustion reaction is illustrated as:

$$Co(NO_3)_2\cdot 6H_2O + \varphi CO(NH_2)_2 + \left(\frac{3\varphi}{2} - \frac{7}{3}\right)O_2 \rightarrow \frac{1}{3}Co_3O_4 + \varphi CO_2\uparrow + (6+2\varphi)H_2O\uparrow + (1+\varphi)N_2\uparrow \quad (1)$$

where, φ is the ratio of total valency of fuel to total valency of oxidizing. To complete the oxidation of fuel (stoichiometric combustion), the amount of φ has been set to 14/9 in which a certain amount of $Co(NO_3)_2\cdot 6H_2O$ and $CO(NH_2)_2$ were added to 25 mL double distilled water (DDW). After 30 min mixing by a magnetic stirrer at 80 °C, the solution was placed in a preheated furnace at 250 °C, at which a fluffy gel was produced and further ignited with a flame followed by a combustion reaction, leading to the corresponding oxides. Additionally, in preparation of Co_3O_4–SnO_2–Sb_2O_3, $CO(NH_2)_2$ was used as fuel, and $Co(NO_3)_2\cdot 6H_2O$ and HNO_3 were used as an oxidizer and combustion aid, respectively. Also, $SnCl_2\cdot 2H_2O$ and $SbCl_3$ were

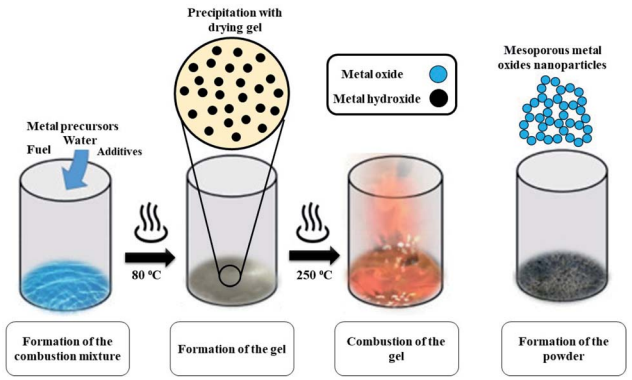

Fig. 1 Schematic diagram of the synthesis of the mixed metal oxides by solution combustion method.

used as precursors. Following reactions also show the mechanism of Co_3O_4–SnO_2–Sb_2O_3 production.

$$Co(NO_3)_2\cdot 6H_2O + 0.1969SnCl_2\cdot 2H_2O + 0.01536SbCl_3 + 0.4398HNO_3\varphi + 1.856CO(NH_2)_2 \rightarrow \frac{1}{3}Co_3O_4 + 0.1969SnO_2 + 0.00768Sb_2O_3 + 1.856\frac{7}{3}CO_2\uparrow + 10.1057H_2O\uparrow + 3.0759N_2\uparrow + 0.43988HCl \quad (2)$$

This reaction is also balanced for stoichiometric combustion. As a result of using the chloride precursors, HNO_3 was used as combustion aid. In order to investigate the effect of thermal annealing on the electrochemical properties of the synthesized metal oxides, calcination processes of the synthesized samples were performed at 400 °C for 2 h.

2.3. Fabrication of composite electrodes

PVDF was first dissolved in DMF to synthesize the CDI electrodes at 50 °C. Next, AC, CB, and the synthesized metal oxides powder were added while stirred for one hour. Following evaporation of the excess solvent at 100 °C, the dense slurries were dropwise cast onto the graphite as the current collector. The fabricated electrodes were coated on graphite (as the substrate) for characterization, electrochemical, and CDI tests with an average mass load of 5 mg cm^{-2}. Finally, the coated electrodes were dried in a fan-forced oven at 110 °C overnight. The corresponding mass ratios of each synthesized electrode are shown in Table 1.

2.4. Electrodes characterization

An Inel Equinox 3000 X-ray diffractometer performed XRD for crystalline phase analysis. The FT-IR spectra were studied using NICOLET 10-Thermo Fisher Scientific (ATR). Further, X-ray photoelectron spectroscopy (XPS) tests were performed for the synthesized nanoparticles. Scanning SEM images of the electrodes were obtained using a VEGA3-TESCAN scanning electron microscope with Energy-dispersive X-ray spectroscopy. Nitrogen sorption isotherms were measured at 77.3 K on an automatic N_2 adsorption/desorption instrument (Quantachrome Autosorb Automated Gas Sorption System), where the samples were outgassed in the vacuum at 300 °C for 3 h before the adsorption/desorption experiment. The BET method and the BJH model were used to obtain specific surface areas and pore size distributions.

Table 1 HECDI electrodes compositions and summarized names

Sample	Active materials	Mass ratio (%)
AC	AC + PVDF	90 : 10
AC/CB	AC + CB + PVDF	80 : 10 : 10
AC/Co_3O_4	AC + CB + Co_3O_4 + PVDF	70 : 10 : 10 : 10
AC/Co_3O_4–Sb_2O_3–SnO_2	AC + CB + (Co_3O_4–Sb_2O_3–SnO_2) + PVDF	70 : 10 : 10 (70 : 2.4 : 27.6) : 10

2.5. Electrochemical characterization of the electrodes

The electrochemical performances and capacitance measurement of the electrodes were evaluated with cyclic voltammetry (CV), galvanostatic charge–discharge (GCD), and electrochemical impedance spectroscopy (EIS) using a potentiostat (Zive sp100- Edaq). All electrochemical tests were conducted by a three-electrode system, consisting of the synthesized electrode, platinum, and Ag/AgCl, as the working, counter, and reference electrodes, respectively, and 1 M NaCl solution as electrolyte. The CV responses of the electrodes were measured at different scan rates varying from 10 to 100 mV s^{-1} and potentials between −0.3 and 0.7 V (*vs.* Ag/AgCl) in a 1 M of NaCl solution. The GCD tests of the electrode were performed at different current densities of 0.2, 0.4, 0.6, 0.8, 1, and 2 A g^{-1} in the potential window of −0.3 to 0.7 V (*vs.* Ag/AgCl) in a 1 M of NaCl solution. Impedance spectroscopy measurements were performed by applying a sinusoidal signal in the frequency range of 0.01 Hz to 10 kHz.

The specific capacity values (C_{CV} (F g^{-1})) of the synthesized composite electrodes were determined using the cyclic voltammetry curve according to eqn (3):[40,41]

$$C_{CV} = \frac{\int_{V_a}^{V_c} I(V)\mathrm{d}V}{mv(V_a - V_c)} \quad (3)$$

The calculated specific capacity (C_{GCD} (F g^{-1})) by the GCD test is according to eqn (4).[42]

$$C_{GCD} = \frac{I \times \Delta t}{m \times \Delta V} \quad (4)$$

where C_{CV} (F g^{-1}) represents the specific capacity by the CV test while C_{GCD} (F g^{-1}) shows the specific capacity by the GCD test; m (g) is the weight of the active materials, Δt is the discharge time, v (V s^{-1}) stands for the sweep rate, and ($V_a - V_c$) and ΔV are the potential window which is between −0.3 and 0.7 V (*vs.* Ag/AgCl).

2.6. CDI experiment

The desalination performances of the electrodes were examined by conducting batch-mode electrosorption experiments using a continuously recycling system. The schematic diagram of this system is presented in Fig. 2. Feed solution (*ca.* 160 mL) was continuously passed through the CDI system using a peristaltic pump at the flow rate of 20 mL min^{-1}. The electrical conductivity and pH of the treated water were determined by the electrical conductivity meter and pH meter, as shown in Fig. 1. Treated effluent was redirected to the feed vessels until the electrical conductivity of the water became constant. Plexiglass sheet (20 cm × 20 cm × 1 cm) with fitting indentations were used as the supporting foundation for the CDI system, and a hallow silicon rubber was used to hold the electrodes separated by 1 mm.

According to eqn (2), the ion removal capacity (IRC) in mg g^{-1} was defined as the number of removed ions per mass of electrode material.[8]

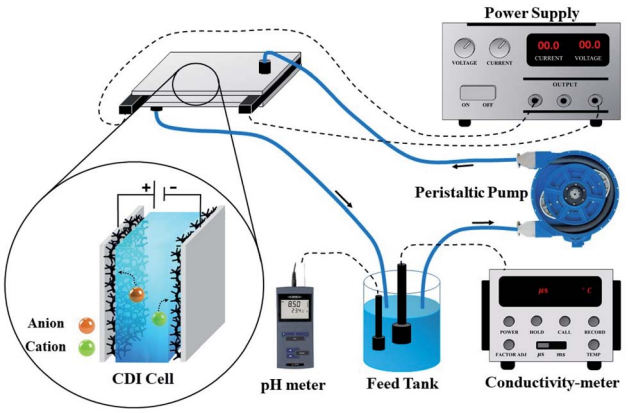

Fig. 2 Schematic diagram of CDI experimental set-up.

$$\mathrm{IRC} = \frac{(C_i - C_f) \times V_s}{m_e} \quad (5)$$

where C_i and C_f represent the initial and final concentration of the solution, respectively, V is the solution volume, and m stands for the mass of the electrodes.

3. Results and discussion

3.1. Characterization of synthesized materials and electrodes

The surface morphologies of the Co_3O_4 and Co_3O_4–SnO_2–Sb_2O_3 nanoparticles are demonstrated by using FE-SEM at different magnifications of 2 and 50 μm, as shown in Fig. 3(a) and (b). Fig. 3(a) and(b) shows the porous structures of Co_3O_4 and Co_3O_4–SnO_2–Sb_2O_3 nanoparticles originated from the solution combustion synthesis. As shown in Fig. 4, the surface morphology and compositions of the synthesized electrodes were analyzed using SEM and EDS, respectively. Fig. 4(a) and (f) show the porous structures of AC/Co_3O_4 and AC/Co_3O_4–Sb_2O_3–SnO_2 nanoparticles resulting from the presence of Co_3O_4 and Co_3O_4–Sb_2O_3–SnO_2 nanoparticles. In addition, a lower degree of agglomeration is found for the coating material, including Sb and Sn, which is in line with the outcomes of the crystallite sizes (see Fig. 5(a)). Moreover, the composition of the electrodes is presented by EDS and elemental mapping (Fig. 4(b)–(e) and (g)–(k)). One can observe that the metal oxides are dispersed homogeneously in the electrode structure. The homogeneous porous structure of AC/Co_3O_4–Sb_2O_3–SnO_2 nanoparticles can provide numerous channels for electrolyte transport which is beneficial for the CDI performance.

Fig. 5(a) shows the XRD patterns of the synthesized samples. In the XRD patterns of as-synthesized Co_3O_4 and annealed Co_3O_4, the peaks at $2\theta = 19.3°$, 31.6°, 37°, 45.2°, 59.5°, 65.5°, are assigned to the diffraction of the crystalline planes with the miller indices of (111), (220), (311), (400), (511) and (440) planes of cubic spinel Co_3O_4 nanoparticles, which are more intense at annealed Co_3O_4 pattern.[43,44] The crystallite size (D) of as-synthesized Co_3O_4 is determined by about 16.65 nm, calculated by the Debye–Scherrer's formula according to the eqn (6):

$$D = K\lambda/\beta \cos\theta \quad (6)$$

where K is the Scherrer constant (commonly taken as 0.9), λ is the average wavelength of the incident X-ray source (1.54178 Å), β is the full width at half maximum, and θ is the Bragg angle.[45] A comparison between annealed Co_3O_4 and as-synthesized Co_3O_4 shows the effect of the calcination process on increasing the crystallite size to 19.51 nm at 400 °C due to the corresponding crystal growth. After composing Co_3O_4 with Sb_2O_3 and SnO_2 (as-synthesized Co_3O_4–Sb_2O_3–SnO_2), the crystallite size decreases to 12.7 nm. Thus, adding Sn and Sb becomes a growth inhibitor to the formation of larger crystals. Moreover, the average crystallite size of annealed Co_3O_4–Sb_2O_3–SnO_2 nanoparticles at 400 °C was calculated by about 14.5 nm. The smaller crystallite size of Co_3O_4–Sb_2O_3–SnO_2 active material provides a higher surface-to-volume ratio and a high available surface area for the ion storage process, which is consistent with the result of BET (see Table 2). In addition, it can be clearly seen that there are no

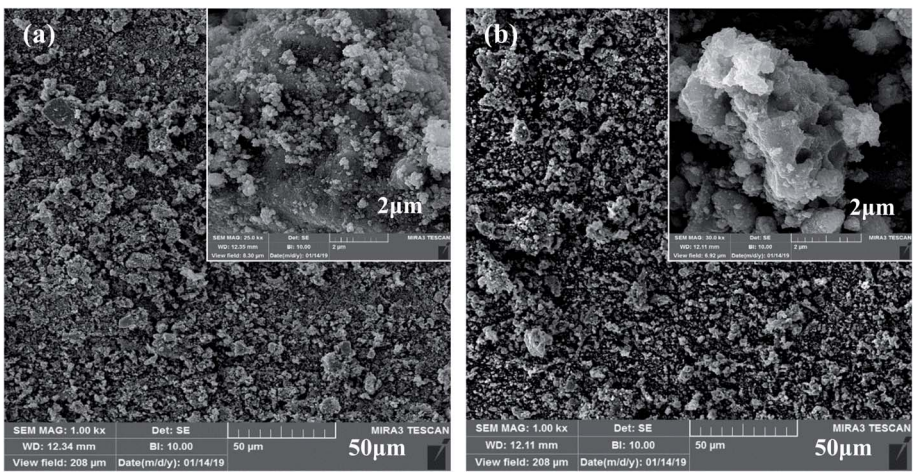

Fig. 3 (a) FE-SEM micrographs of Co_3O_4 nanoparticles with different magnifications of 2 and 50 μm, (b) FE-SEM micrographs of Co_3O_4–Sb_2O_3–SnO_2 nanoparticle with different magnifications of 2 and 50 μm.

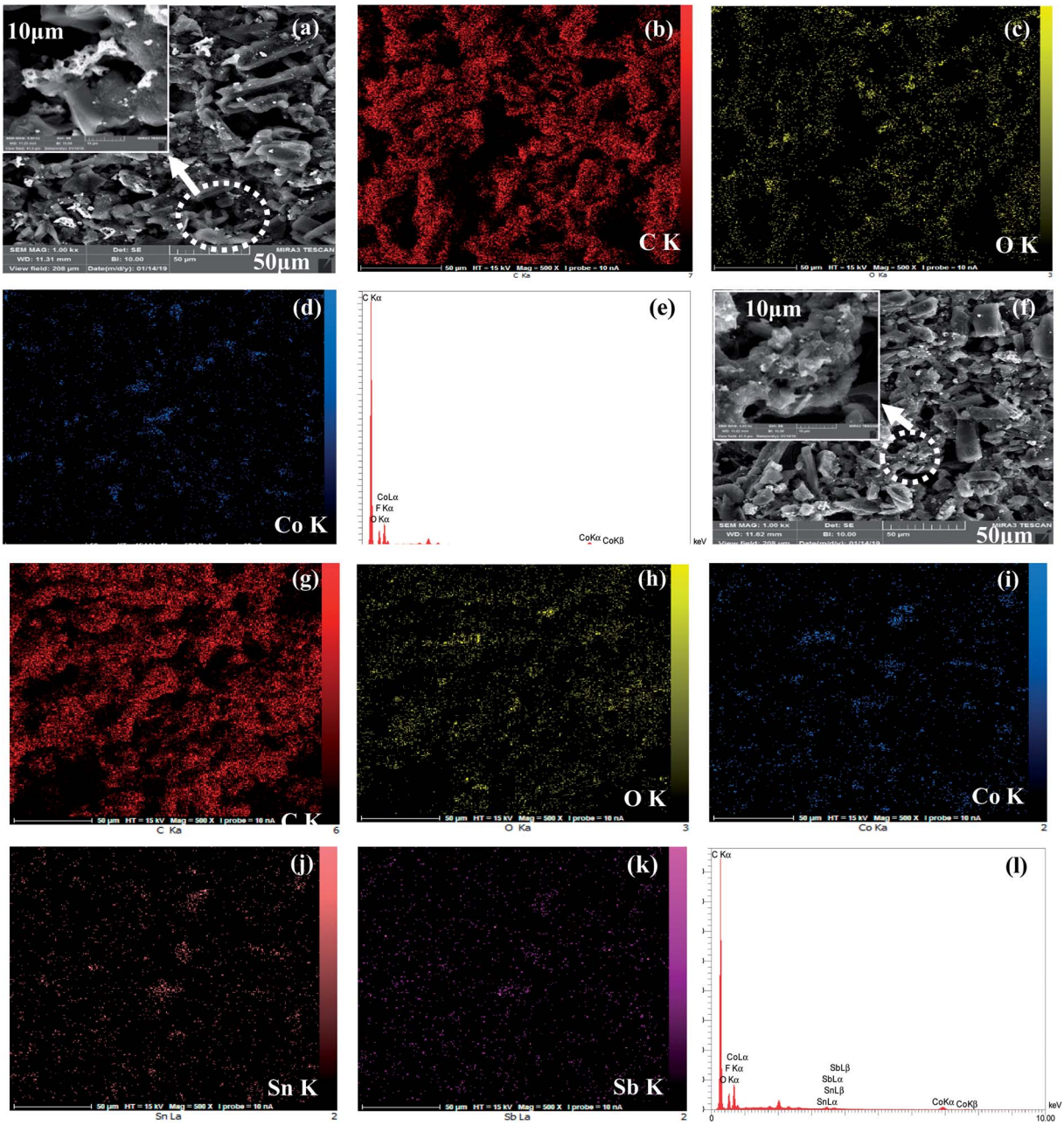

Fig. 4 SEM micrographs of AC/Co_3O_4 electrode (a–d), (a) SEM image at low resolution (50 µm) and higher resolution (10 µm), (b) C (carbon) mapping, (c) O (oxygen) mapping, (d) Co (cobalt), (e) EDS elemental diagram of AC/Co_3O_4 electrode. SEM micrographs of AC/Co_3O_4–Sb_2O_3–SnO_2 electrode (f–k), (f) SEM image at low resolution (50 µm) and higher resolution (10 µm) and elemental mapping of (g) C, (h) O, (i) Co, (j) Sn (tin), (k) Sb (antimony), and (l) EDS elemental diagram of AC/Co_3O_4–Sb_2O_3–SnO_2 electrode.

diffraction peaks related to Sn and Sb, which is due to the non-crystalline nature of the Co_3O_4–Sb_2O_3–SnO_2 nanoparticles.

The chemical composition of the synthesized electrodes was characterized by FT-IR spectroscopy, as shown in Fig. 5(b). The two peaks at 570 cm^{-1} and 663 cm^{-1} correspond to the Co–O vibrations for all the synthesized samples.[44–46] The molecular vibrations between 600 and 680 cm^{-1} indicate the fundamental stretching vibration of Sn–O and Sn–O–Sn in the as synthesized and annealed Co_3O_4–Sb_2O_3–SnO_2 nanoparticles.[47] The peak at 739 cm^{-1} is attributed to the Sb–O vibration.[48] The peaks around 1550–1650 cm^{-1} and 2800–3000 cm^{-1} correspond to the bending vibration of absorbed molecular water and stretching vibrations of the OH group.[44]

The nitrogen adsorption–desorption isotherms and the BJH pore-size distribution of all the synthesized active materials are shown in Fig. 6. The isotherms of as-synthesized Co_3O_4, annealed Co_3O_4, as-synthesized Co_3O_4–Sb_2O_3–SnO_2, and annealed Co_3O_4–Sb_2O_3–SnO_2 are shown from Fig. 6(a) to 4(d), respectively, which can be categorized as type IV according to the IUPAC classification.[49]

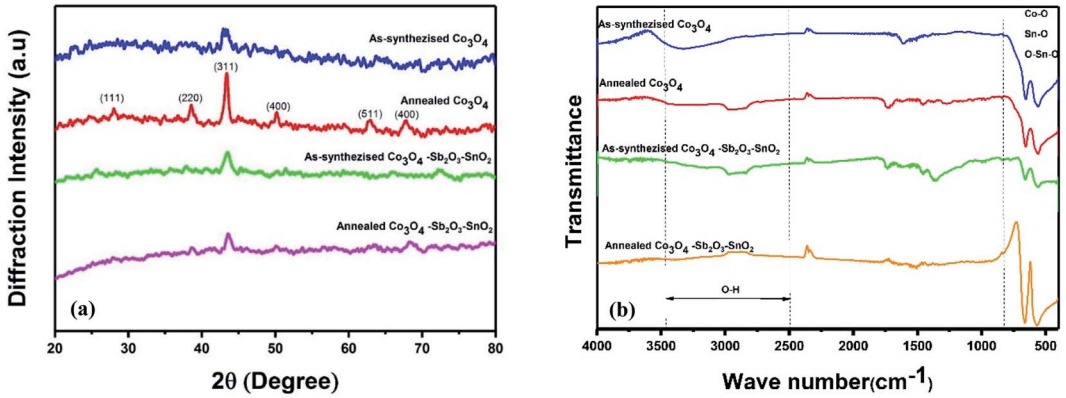

Fig. 5 (a) XRD patterns of as-synthesized and annealed nanoparticles. (b) FT-IR spectrums of as-synthesized and annealed nanoparticles.

The specific BET surface areas, average pore sizes, and total pore volumes of the synthesized nanopowders are listed in Table 2. The result shows that the pore size of as-synthesized and calcined nanopowders is in the range of mesoporous (between 2 and 50 nm).[15] It can be seen that the total pore volume for as-synthesized and annealed Co_3O_4 is greater than as-synthesized and annealed Co_3O_4–Sb_2O_3–SnO_2 nanopowders, the broader pore size distribution in their structures leading to larger average pore size. However, the higher surface areas of the as-synthesized and annealed Co_3O_4–Sb_2O_3–SnO_2 nanopowders can be attributed to their more mesoporous structure with greater ion-accessible sites. This can increase the specific capacitance and ion removal capacity by providing more available sites to proceed with the pseudocapacitive reaction.[50] As a result, the AC/Co_3O_4–Sb_2O_3–SnO_2 electrode displays efficient desalination using EDL and pseudocapacitive mechanisms.

The elemental composition and electronic states of the Co_3O_4–Sb_2O_3–SnO_2 nanopowder were investigated by XPS analysis, as demonstrated in Fig. 7. The Co 2p XPS spectra display a doublet with binding energies at 779.8 and 794.8 eV, corresponding to Co $2p_{3/2}$ and Co $2p_{1/2}$ (Fig. 7(a)), which are the characteristics of the Co_3O_4 phase.[51] Furthermore, the high-resolution Sn 3d spectra of the Co_3O_4–Sb_2O_3–SnO_2 nanopowder represent two symmetric doublet peaks are centered at 486.2 and 494.7 eV related to Sn $3d_{5/2}$ and Sn $3d_{3/2}$, indicating the presence of Sn in the oxidation of +4 (Fig. 7(b)).[52] The Sb $3d_{5/2}$ and Sb $3d_{3/2}$ peaks at 529.9 and 539.2 are assigned to Sb^{3+}, which illustrate the presence of Sb_2O_3 in Co_3O_4–Sb_2O_3–SnO_2 nanopowder (Fig. 7(c)).[53] As shown in Fig. 7(d), there are two distinct peaks. Precisely, the peak at 530.1 eV corresponds to the binding between oxygen and metal atoms, the peak at 531.2 eV is attributed to the oxygen vacancies.[54]

3.2. Electrochemical properties

In order to characterize the electrochemical properties of the synthesized electrodes, CV and EIS techniques were employed. Fig. 8(a) shows the typical CV curves of the electrodes at the scan rate of 10 mV s^{-1} in 1 M NaCl electrolyte solution. According to the quasi-rectangular shapes of the diagrams without any prominent redox peaks, an excellent electrochemical double layer (EDL) capacitance behavior can be implied. Besides, symmetric voltammogram concerning the *x*-axis indicates a highly reversible capacitive behavior of the electrodes.[55–57] The CV specific capacities for CDI electrodes were calculated by 33, 68, 96, and 124 F g^{-1} at the scan rate of 10 mV s^{-1} for AC, AC/CB, AC/Co_3O_4, AC/Co_3O_4–Sb_2O_3–SnO_2 electrodes, respectively. It could be clearly seen that the AC/Co_3O_4–Sb_2O_3–SnO_2 electrode reveals a remarkable improvement in AC capacitance due to the synergic effects resulting from pseudo-capacitance behavior of Co_3O_4–Sb_2O_3–SnO_2 and EDLs property from AC.

Moreover, the Co_3O_4–Sb_2O_3–SnO_2 nanopowder shows the most specific surface area (see BET analysis in Table 2) among all the synthesized materials. Hence, the mesopore nanopowder of Co_3O_4–Sb_2O_3–SnO_2 with a higher specific surface area improves the capacitive performance of AC/Co_3O_4–Sb_2O_3–SnO_2 electrode by increasing the accessible sites for the ion adsorption, leading to a higher specific capacity. The CV results in Fig. 8(a) also show that carbon black in the composite structure can improve electronic conductivity, decreasing charge transfer resistance. This result is consistent with the result of charge

Table 2 Microstructure parameters obtained by BET analysis of the samples

Samples	BET (m^2 g^{-1})	Average pore size (nm)	Total pore volume (cm^3 g^{-1})
As-synthesized Co_3O_4	54.60	15.40	0.2101
Annealed Co_3O_4	27.12	24.88	0.2487
As-synthesized Co_3O_4–Sb_2O_3–SnO_2	99.82	6.34	0.1456
Annealed Co_3O_4–Sb_2O_3–SnO_2	91.63	8.01	0.1835

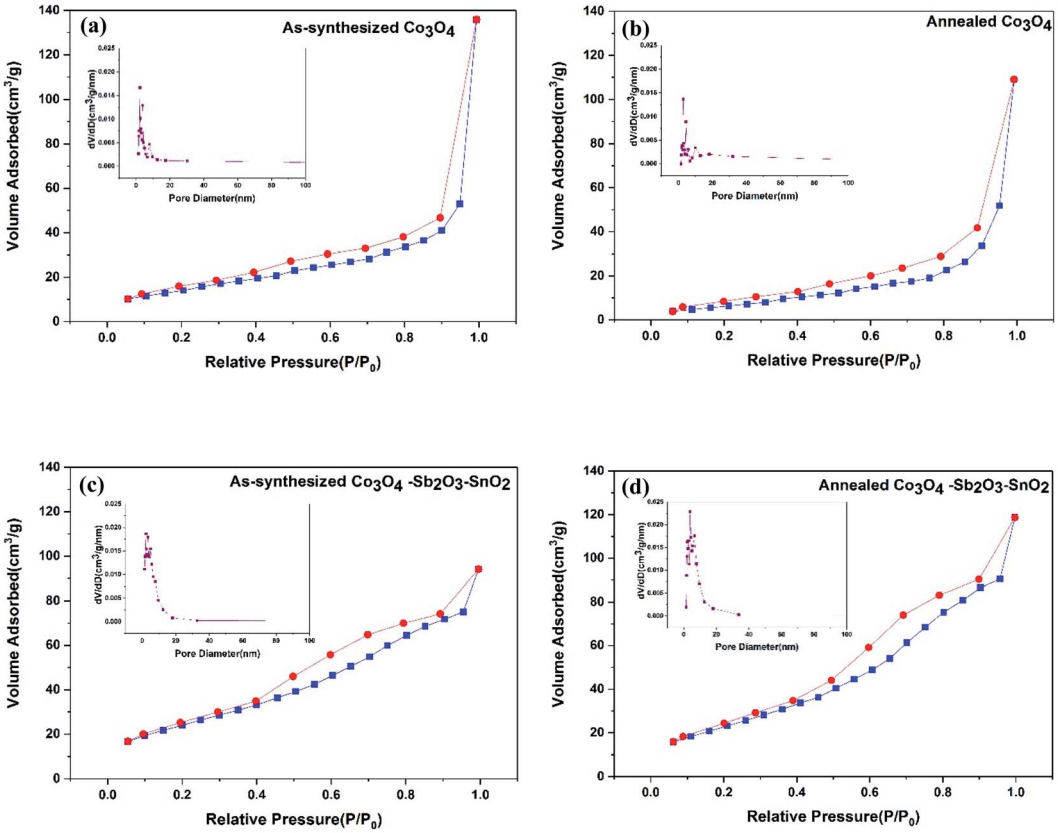

Fig. 6 Nitrogen adsorption/desorption isotherm BJH pore-size distribution (a) as-synthesized Co_3O_4 (b) annealed Co_3O_4 (c) as-synthesized Co_3O_4–Sb_2O_3–SnO_2 and (d) annealed Co_3O_4–Sb_2O_3–SnO_2 nanoparticles.

transfer resistance in the EIS plot (see Fig. 8(g)), resulting in a higher current density in the voltammograms of AC/CB composites (Fig. 8(a)). As shown in Fig. 8(b), the decline of the specific capacity as a function of the scan rate is attributed to the insufficient time of EDL formation and the emergence of the pseudo-capacitive behavior of the electrodes. Besides, the AC/Co_3O_4–Sb_2O_3–SnO_2 electrode shows the highest specific capacity in the scan rates between 10 and 100 mV s^{-1} (see Fig. 8(b)).

Fig. 8(c) demonstrates the capacity retention of the electrodes. The AC/Co_3O_4–Sb_2O_3–SnO_2 electrode displays the highest capacity retention of 47.5% at the scan rate of 100 mV s^{-1}, indicating the higher rate capability and faster charge storage process of the electrode. The higher rate capability of the AC/Co_3O_4–Sb_2O_3–SnO_2 electrode originates from the more pseudo-capacitive reaction in the surface of the electrode because of the more accessible sites or available surface area of the Co_3O_4–Sb_2O_3–SnO_2 nanopowder.

In order to represent the effect of SnO_2 as a promising cycling stability agent, the specific capacity of the electrodes was carried out at a high scan rate of 100 mV s^{-1} for 2000 cycles. As shown in Fig. 8(d), the specific capacity of AC, AC/CB electrodes are reserved 86.9 and 90.7% of its initial specific capacities after 2000 cycles, respectively. After adding Co_3O_4 for AC/Co_3O_4 electrode, the capacity retention decreases to 76.3% due to the poor cycling stability of Co_3O_4. On the other hand, the AC/Co_3O_4–Sb_2O_3–SnO_2 electrode is maintained 97.2% of initial specific capacity, indicating the excellent stability of the AC/Co_3O_4–Sb_2O_3–SnO_2 electrode, which originates from the high cycling stability of the SnO_2 nanopowder.[35]

Fig. 8(e) shows the typical charge–discharge curves of the electrodes at a potential sweep window from −0.3 to 0.7 V (*vs.* Ag/AgCl) at a current density of 0.2 A g^{-1}. In line with the CV results, the AC/Co_3O_4, AC/Co_3O_4–Sb_2O_3–SnO_2 electrodes represent a much longer discharge time than AC and AC/CB electrodes, indicating the higher specific capacity of AC/Co_3O_4 and AC/Co_3O_4–Sb_2O_3–SnO_2 electrodes. It can be found that the GCD profile is non-linear for AC/Co_3O_4 and AC/Co_3O_4–Sb_2O_3–SnO_2 electrodes, suggesting the pseudocapacitive nature of charge storage for these electrodes. The specific capacities of the electrodes derived from the discharge curves at current densities of 0.2, 0.4, 0.6, 0.8, 1, and 2 A g^{-1} (see Fig. 8(f)). The specific capacities calculated by discharge time are 33.8, 67.4, 115.7, and 141.2 F g^{-1} for AC, AC/CB, AC/Co_3O_4, and AC/Co_3O_4–Sb_2O_3–SnO_2 electrodes, at the current density of 0.2 A g^{-1}. The results reveal that the AC/Co_3O_4–Sb_2O_3–SnO_2 electrode exhibits a much higher specific capacity than other electrodes at all current densities.

The EIS analysis was used to examine further the electrochemical capacitive and kinetics of the synthesized electrodes. The Nyquist plots of the electrodes at frequencies from 0.01 Hz to 10 kHz are presented in Fig. 5(e). It is known that the Nyquist

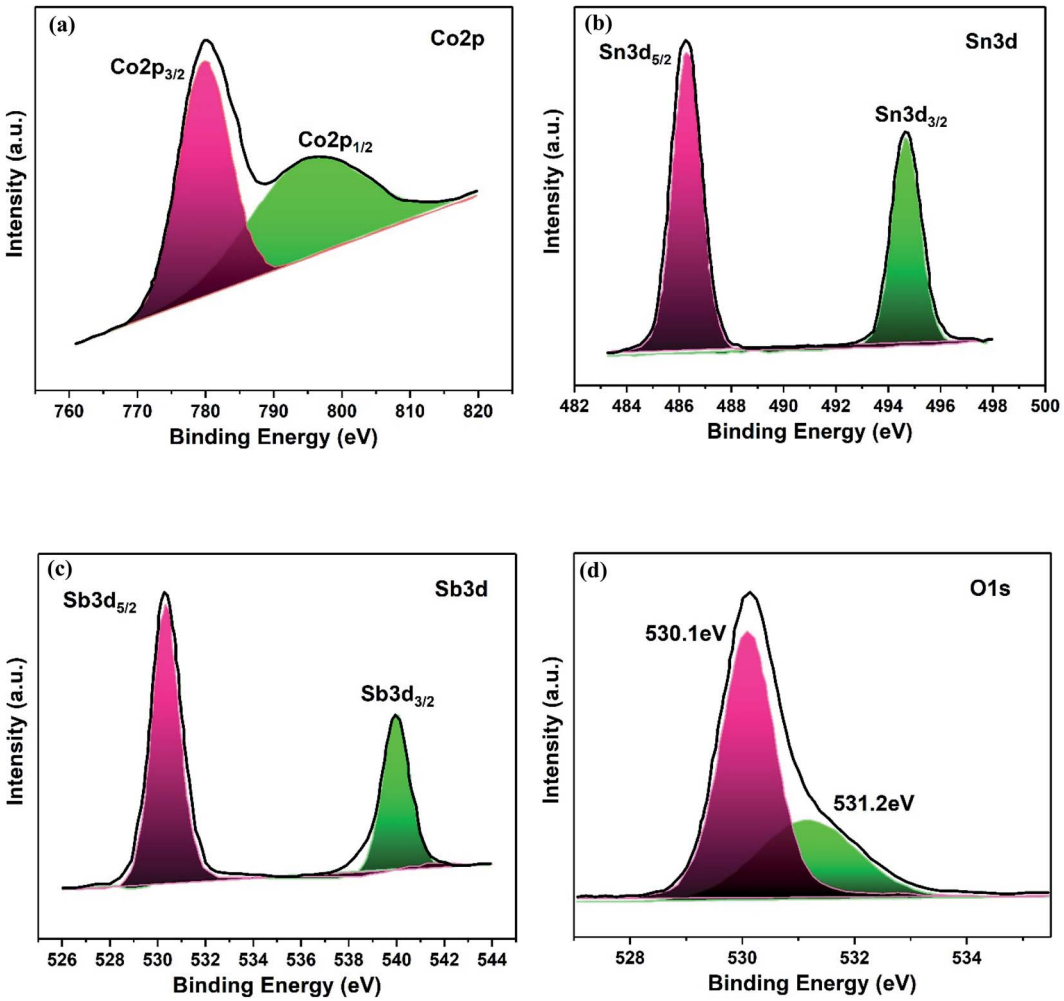

Fig. 7 XPS spectra of Co_3O_4–Sb_2O_3–SnO_2 nanoparticle, (a) Co 2p, (b) Sn 3d, (c) Sb 3d and (d) O 1s.

plots are divided into three sections: (1) the high-frequency intercept on the real Z' axis indicates the bulk electrolyte resistance (R_s). Namely, such resistance includes the ionic resistance of electrolyte (2), the diameter of the small semicircle displayed at high-frequency region demonstrates the charge transfer resistance (R_{ct}) at the interface of the electrode and electrolyte, and (3) the linear zone at the low-frequency region is attributed to the diffusion impedance resulting from the mass transfer resistance in the system.[48] Simultaneously, the EIS data were fitted to an equivalent electric circuit (EEC), and the fitting procedure demonstrates good compliance between theoretical and experimental data by using R_s, R_{ct}, and a constant phase element (CPE – Q_{dl} and exponent n). The EIS data simulation results are presented in Table 3. It can be observed that after adding CB to the AC electrode, the R_{ct} decreases from 156.4 to 9.7 Ω since CB enhances the electrical conductivity of the electrode. By adding the Sb_2O_3 as an electrical conductivity promoter, the AC/Co_3O_4–Sb_2O_3–SnO_2 electrode shows an excellent electrical conductivity with R_{ct} of 2.6 Ω.

In addition, in the low-frequency region, the slope of the curve corresponding to the AC/Co_3O_4–Sb_2O_3–SnO_2 electrode is significantly greater than the other electrodes (as shown in Fig. 8(g)). The AC/Co_3O_4–Sb_2O_3–SnO_2 electrode shows the highest Q_{dl} and n values of 635 μF s^{n-1} and 0.93, respectively, indicating a lower diffusion resistance and an ideal electrical double layer capacitance, suggesting faster ion diffusion and confirming the improvement of capacity for AC/Co_3O_4–Sb_2O_3–SnO_2 electrode.[58] The lowest R_s of 2.9 Ω assigned to the AC/Co_3O_4–Sb_2O_3–SnO_2 electrode points out the respective active material's superior conductivity and the minimum contact resistance with the current collector. In light of the discussed results, it can be stated that the AC/Co_3O_4–Sb_2O_3–SnO_2 electrode facilitates the charge transfer with the reduced contact resistance due to the homogeneous structure of the electrode with high ion accessible sites.

In order to analyze the proportion of the capacitive and (K_1v) diffusion ($K_2v^{0.5}$) control charge storage processes, following equation, have been used:[59]

$$i(V) = K_1v + K_2v^{0.5} \quad (7)$$

where $i(V)$ is the measured current at a fixed potential (V) under a certain sweep rate, K_1 and K_2 are adjustable values. The

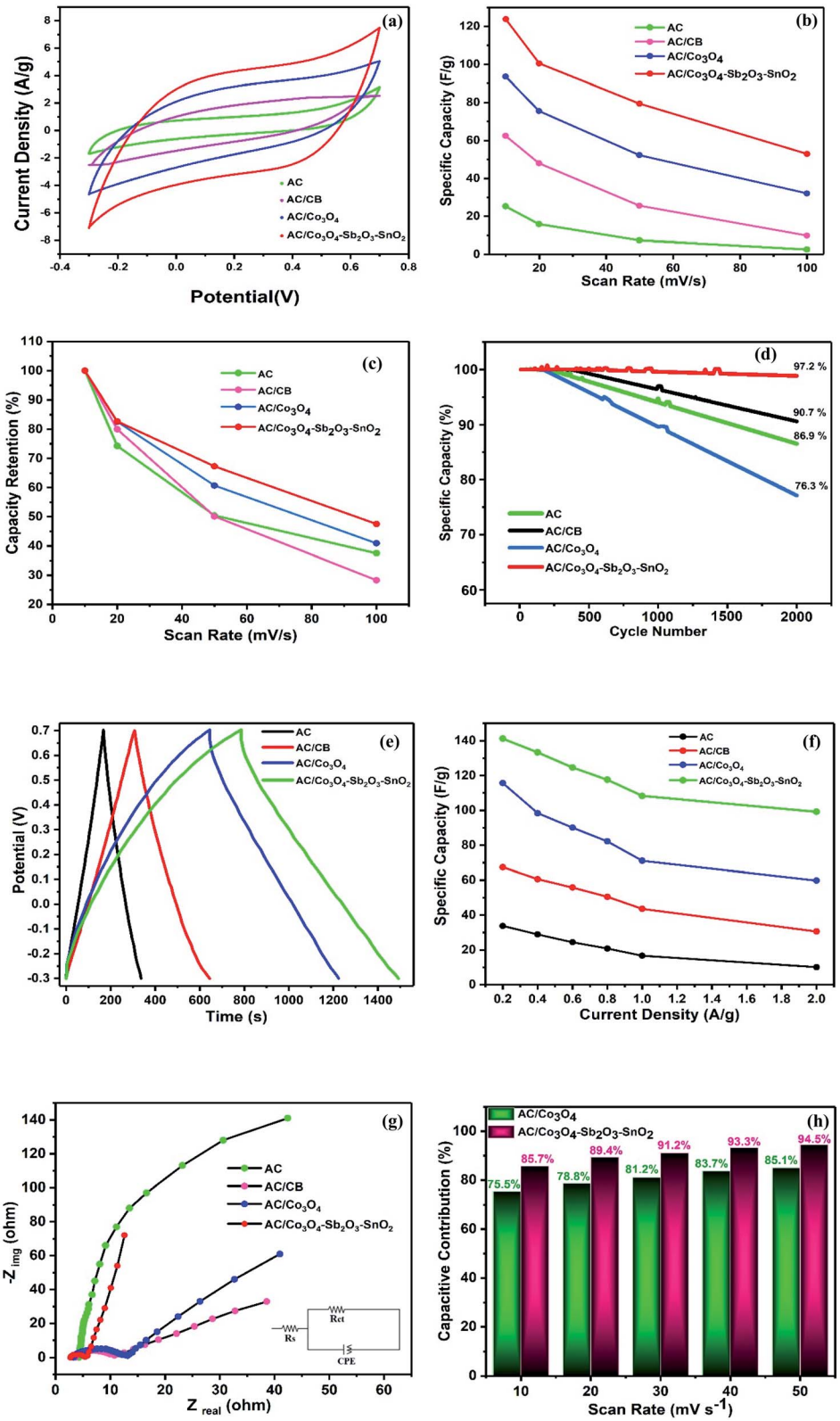

Fig. 8 CV of (a) all synthesized electrodes at the scan rate of 10 mV s^{-1}, (b) calculated specific capacity of the developed electrodes at different scan rates, (c) capacity retention of the developed electrodes at different scan rates, and (d) specific capacity (%) after 2000 cycles at the scan rate of 100 mV s^{-1}, (e) GCD of all synthesized electrodes at the current density of 0.2 A g^{-1}, (f) calculated specific capacity of the developed electrodes at different current densities, (g) Nyquist plots of all electrodes, (h) capacitive contribution (%) of the AC/Co_3O_4 and AC/Co_3O_4–Sb_2O_3–SnO_2 electrodes.

Table 3 EIS data simulation for all CDI electrodes in 1 M NaCl solution; fitted to the EEC inset to Fig. 8(d)

Samples	R_s (Ω)	R_{ct} (Ω)	Q_{dl} (μF s^{n-1})	N
AC	4.2	156.4	187	0.62
AC/CB	3.7	9.7	212	0.54
AC/Co_3O_4	3.5	11.3	456	0.79
AC/Co_3O_4–Sb_2O_3–SnO_2	2.9	2.6	635	0.93

capacitive contribution factor of the AC/Co_3O_4 and AC/Co_3O_4–Sb_2O_3–SnO_2 electrodes has been calculated using eqn (7) at scan rates of 10, 20, 30, 40, and 50 mV s^{-1}. As illustrated in Fig. 8(h), both AC/Co_3O_4 and AC/Co_3O_4–Sb_2O_3–SnO_2 electrodes show high capacitive contribution factors at all scan rates, indicating surface-capacitive processes play a leading role in the charge storage process of these electrodes. It can be clearly seen that the AC/Co_3O_4–Sb_2O_3–SnO_2 electrode represents a higher capacitive contribution factor, demonstrating a higher pseudocapacitive charge storage reaction of this electrode, which is originated from the higher active sites and surface area of the AC/Co_3O_4–Sb_2O_3–SnO_2 electrode (see BET results in Fig. 6 and Table 2).

3.3. Desalination performance in CDI system

The desalination performances of the synthesized electrodes were studied in a batch mode experiment while applying a cell voltage of 1.6 V. Potable water (160 mL) was pumped into the reactor in a mixing mode for about 60 min where the conductivity of the solution was recorded *versus* time. The experiments were performed for potable water with initial electrical conductivity of 550 μs cm^{-1}. Fig. 9(a) illustrates the change in the solution conductivity of the various electrode materials. When a cell voltage of 1.6 V is applied on the CDI electrodes, the conductivity of AC and AC/CB decreases, and a drastic drop in the solution conductivity of AC/Co_3O_4 and AC/Co_3O_4–Sb_2O_3–SnO_2 can be observed, indicating the adsorption of salt ions from the aqueous solution which subsequently forms the EDL. The desalination is conducted until reaching ion-storage saturation. The final conductivity of the solution for AC, AC/CB, AC/Co_3O_4, and AC/Co_3O_4–Sb_2O_3–SnO_2 electrodes are determined about 521, 509, 486, and 458 μs cm^{-1}. The AC and AC/CB electrodes show a typical desalination behavior during deionization. In contrast, the AC/Co_3O_4 and AC/Co_3O_4–Sb_2O_3–SnO_2 electrodes result in a superior desalination performance, indicating high ion accessible sites attributed to the high respective available surface area (see Fig. 6).

Fig. 9(b) demonstrates the variation of ion removal capacity as a function of time. The AC, AC/CB, and AC/Co_3O_4 electrodes demonstrate the ion removal capacity of 10, 14, and 24 mg g^{-1}, whereas AC/Co_3O_4–Sb_2O_3–SnO_2 electrode reveals the maximum ion removal capacity of 34 mg g^{-1}, under the same operating condition. It is clear that adding Co_3O_4, Sb_2O_3, and SnO_2 to the electrode material improves the ion removal capacity where the AC/Co_3O_4–Sb_2O_3–SnO_2 electrode displays a superior desalination rate as compared to the other electrode materials. The excellent adsorption efficiency of the AC/Co_3O_4–Sb_2O_3–SnO_2 electrode can be related to (i) incorporation of Co_3O_4–Sb_2O_3–SnO_2 to AC leads to the porous structure and a lower degree of agglomeration in AC/Co_3O_4–Sb_2O_3–SnO_2 electrode which increases the specific surface area and provides ions diffusion easily through intra-channel pathway on the electrode surface, (ii) a promising tuning of the porous structure of the latter active material and (iii) higher specific capacitance and lower charge transfer resistance of AC/Co_3O_4–Sb_2O_3–SnO_2 electrode which were inferred from the EIS test. To investigate the effect of voltage on the IRC of the CDI system, deionization experiments were conducted at different voltages, as shown in Fig. 9(c). Applying the cell voltages of 1.2, 1.4, and 1.6 V result in the IRC of 21, 23, and 27 mg g^{-1}, respectively, for the AC/Co_3O_4 electrode, while the IRC was measured by 23, 25, and 34 mg g^{-1} for AC/Co_3O_4–Sb_2O_3–SnO_2 electrode, respectively. Such increases result from greater electrosorption capacity and reaction rate resulting from strong electrostatic forces at higher voltages.[6,7]

The effect of the initial conductivity of potable water on the IRC was also investigated in the CDI system for the electrode materials of AC/Co_3O_4 and AC/Co_3O_4–Sb_2O_3–SnO_2, as shown in Fig. 9(d). The IRC of the AC/Co_3O_4 at 1.6 V is determined by 19, 29, and 40 mg g^{-1} for the potable water with the conductivity of 350, 650, and 950 μs cm^{-1}, respectively. The IRC of the AC/Co_3O_4–Sb_2O_3–SnO_2 electrode was measured by 22, 35, and 52 mg g^{-1}, respectively, under the same condition. As the initial conductivity of potable water increases, forming a compressed electrical double layer enhances the diffusion of ions inside the pores, consequently reducing the ion insertion resistance and providing good accessibility for the ions.[60,61]

Representing the variation of effluent pH is a promising method to investigate the presence of electrode reactions in CDI cells. A considerable pH variation can be observed when oxidization, reduction, or water splitting reactions occur at the surface of the electrodes.[62] For example, reducing dissolved oxygen in water can increase the pH in the electrolyte. Besides, the high applied voltage can conduct carbon redox reactions where the carbon oxidation can diminish the stability of the electrode.[63] Fig. 10 shows the changes in the effluent pH during the desalination process at the highest voltage of 1.6 V with initial conductivity of 950 μs cm^{-1}. However, it can clearly be seen that there is no significant pH variation for all electrodes at the voltage of 1.6 V, but according to the literature, the pH variation is inevitable during the CDI process. Therefore, slightly acidic pH can be observed in the first 20 min of the desalination process for all the synthesized electrodes, which can be related to the acidic functional groups of the AC or different transport and adsorption/desorption rate of H^+ and OH^- during a CDI cycle.[64] Thus, concerning small pH changes that occurred during desalination, it can be inferred that there is no oxygen reduction and carbon oxidation reaction. In our experiment, the optimum voltage was 1.6 V, but no oxygen bubbles were observed during the experiment, and the weight loss of the electrodes was negligible. Although the high cell voltage typically leads to water splitting on the electrode,[65] the electrode potential is more important than the potential difference between cathode and anode, so that the applied

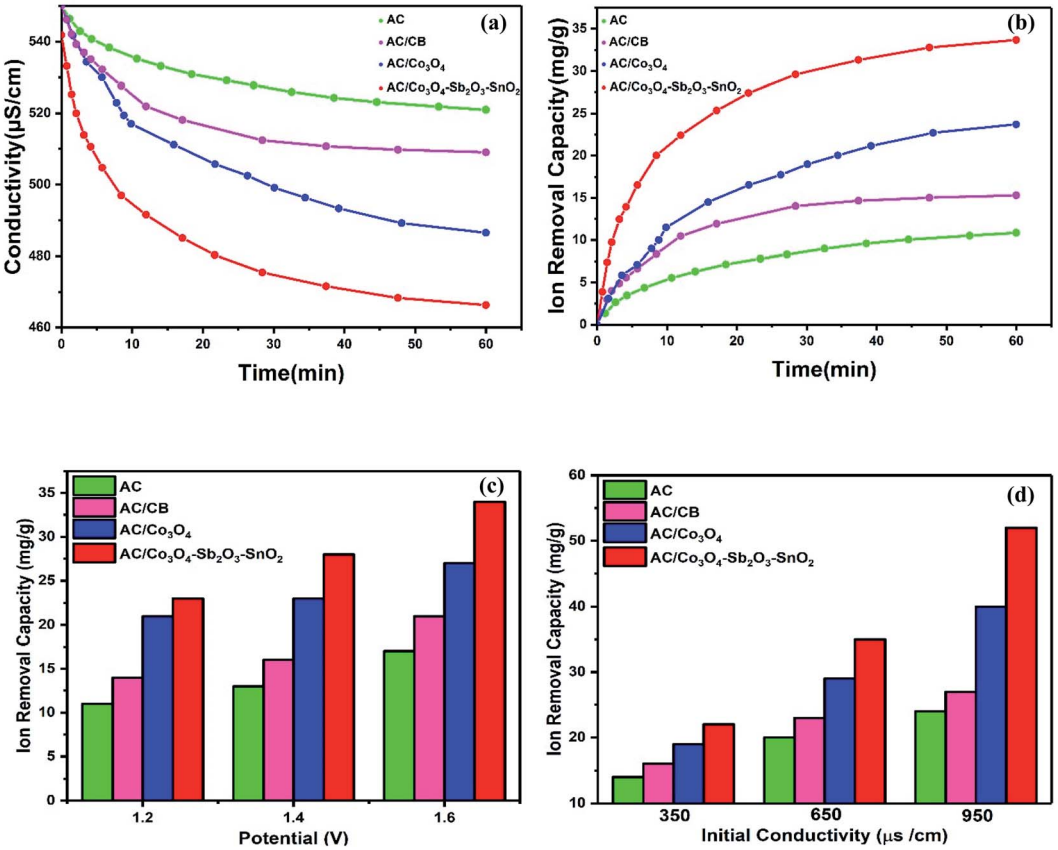

Fig. 9 (a) Variation in conductivity for different HECDI electrodes (at 1.6 V and 550 µs cm^{-1}), (b) change in ion removal capacity for different HECDI electrodes (at 1.6 V and 550 µs cm^{-1}), (c) effect of applied voltage for AC, AC/CB, AC/Co_3O_4 and AC/Co_3O_4–Sb_2O_3–SnO_2 electrodes (1.2 V, 1.4 V, 1.6 V, and 550 µs cm^{-1}), (d) influence of initial conductivity (350, 650 and 950 µs cm^{-1}) for AC, AC/CB, AC/Co_3O_4 and AC/Co_3O_4–Sb_2O_3–SnO_2 HECDI systems and at 1.6 V.

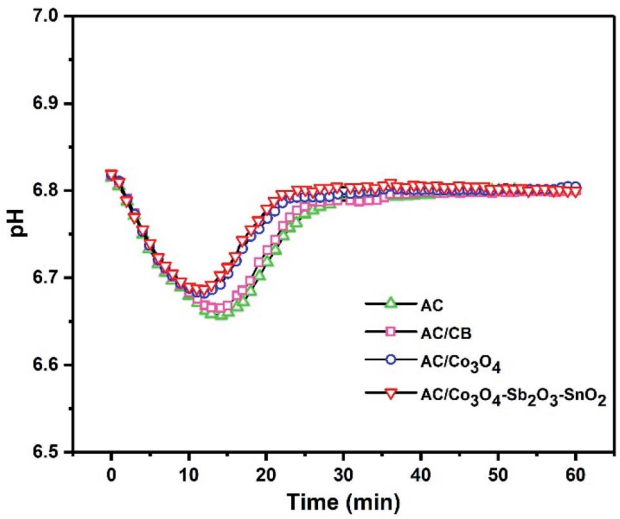

Fig. 10 Effluent pH as a function of time at a cell voltage of 1.6 V with initial conductivity 950 µs cm^{-1}.

potential of the electrode considerably drops depending on series resistance of CDI cell components, including current collectors, electrode material, polymeric binder and wires, and this potential does not inevitably can direct the faradaic reaction.[66]

The ion removal rate is the ion removal capacity of the electrodes per operation time (mg g^{-1} min^{-1}). As shown in Fig. 11(a), the maximum ion removal rate of the AC, AC/CB, AC/Co_3O_4, and AC/Co_3O_4–Sb_2O_3–SnO_2 electrodes at the applied voltage of 1.6 V are 1.8, 2.3, 3.9, and 7.1 mg g^{-1} min^{-1}, respectively. It can be seen that the CDI system with AC/Co_3O_4–Sb_2O_3–SnO_2 electrode shows a superior ion removal rate compared to the other electrode materials. This result displays the faster ion insertion of the AC/Co_3O_4–Sb_2O_3–SnO_2 electrode, which originates from higher ion-accessible sites and specific surface areas. This was already concluded from the BET results. As demonstrated in Fig. 11(b), to explore the desalination–regeneration ability of AC/Co_3O_4–Sb_2O_3–SnO_2 electrode, an electrosorption–desorption experiment has been performed between 1.6 V and 0 V for 100 cycles for the potable water of 573 µs cm^{-1}. A potential difference of 1.6 V was applied for 60 min in the charging step, while a potential of 0 V was applied for 60 min in the discharging step. It can be seen that the conductivity of the solution decreases from 573 to 520 µs cm^{-1} during the desalination and returns to its initial value during the regeneration step. Besides, by adding SnO_2 as a good cycling stability agent, the electrode retains about 99.5% of its ion

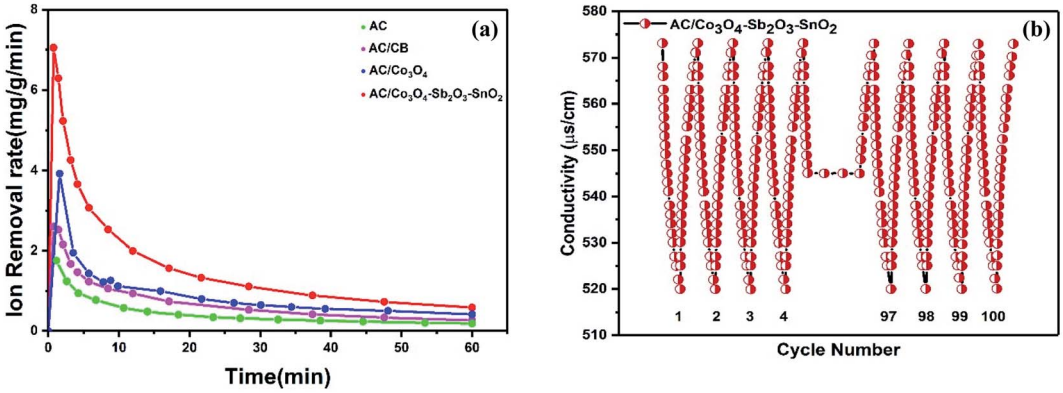

Fig. 11 (a) Change in ion removal rate in four different HECDI systems at 1.6 V and initial concentration of 550 μs cm^{-1}, (b) desalination–regeneration cycles of AC/Co_3O_4–Sb_2O_3–SnO_2 electrode at 573 μs cm^{-1} and 1.6 V.

Table 4 Comparison of IRC of carbon/metal oxide composites based in recently published HECDI systems

Active material	Initial concentration or initial conductivity	*V*	Ion removal capacity (mg g^{-1})	Ref.
Graphene aerogel (GA)–TiO_2	6000 mg L^{-1}	1.2	24.2	24
Graphene–Co_3O_4	250 mg L^{-1}	1.6	18.63	6
AC–TiO_2	584.4 mg L^{-1}	1.2	17	22
ZrO_2–AC	104 mg L^{-1}	1.2	16.35	27
Graphene–Fe_3O_4	300 μs cm^{-1}	1.6	10.30	25
AC–MnO_2	584 mg L^{-1}	1.0	9.3	26
ACC–ZnO	100 mg L^{-1}	1.2	8.5	21
Graphene–SnO_2	N.A.	1.4	1.49	28
AC/Co_3O_4	950 μs cm^{-1}	1.6	40	Present work
AC/Co_3O_4–Sb_2O_3–SnO_2	950 μs cm^{-1}	1.6	52	Present work

removal capacity even after 100 cycles. This result shows that the hybrid electrode of AC/Co_3O_4–Sb_2O_3–SnO_2 can be completely regenerated and reused for ten cycles and reveals excellent desalination–regeneration capability.

Furthermore, the AC/Co_3O_4 and AC/Co_3O_4–Sb_2O_3–SnO_2 electrodes revealed a considerable ion removal capacity compared to the several reported carbon/metal oxide-based CDI and HECDI systems (Table 4). The much more IRC enhancement in the present work than the other reports by fabricating carbon/metal oxide electrodes with a low percent of metal oxide should also appreciate the quite cost-effective developed active material. The IRC of 52 mg g^{-1} (for AC/Co_3O_4–Sb_2O_3–SnO_2 electrode) in this work is about 3.9 and 2.1 times greater than the average (13.22 mg g^{-1}) and highest (24.2 mg g^{-1}) values of the selected eight reported carbon/metal oxide-based materials.

4. Conclusion

Brackish water desalination *via* capacitive deionization is an energy-efficient desalination method. Therefore, the preparation of suitable, cost-effective electrodes is an important consideration which can boost the efficiency of CDI systems. In this study, AC/Co_3O_4 and AC/Co_3O_4–Sb_2O_3–SnO_2 were successfully prepared and examined as the new carbon–metal oxide electrode materials for the HECDI system. The AC/Co_3O_4 and AC/Co_3O_4–Sb_2O_3–SnO_2 electrodes in the HECDI system demonstrated higher ion removal capacity of 40 and 52 mg g^{-1}, respectively, compared to the other carbon–metal oxide-based materials for treating 950 μs cm^{-1} potable water at the applied potential of 1.6 V. The highest ion removal rate was found to be 7.1 mg g^{-1} min^{-1} for the of AC/Co_3O_4–Sb_2O_3–SnO_2 electrode. The presence of SnO_2 in the active material illustrated a good effect on cycling stability, and the AC/Co_3O_4–Sb_2O_3–SnO_2 electrode preserved 99.5% of its initial ion removal capacity after 100 cycles, demonstrating excellent electrochemical stability and desalination/regeneration capability. Moreover, the small amount of Sb_2O_3 (0.24% in active material) as a conductivity promoter could exclude the negative effect of the polymeric binder on the electrical conductivity of the active material. The main advantages of the AC/Co_3O_4–Sb_2O_3–SnO_2 electrode for the CDI technology were found to rely on the high ion removal capacity, high ion removal rate, high desalination–regeneration stability, and excellent electrical conductivity, which are counted as the essential parameters to use the CDI technology in a larger scale.

Author contributions

Ehsan Delfani: data curation, formal analysis, investigation, methodology, validation, writing – original draft. Alireza

Khodabakhshi: data curation, formal analysis, investigation, methodology, validation. Sajjad Habibzadeh: conceptualization, funding acquisition, writing – review & editing, project administration, resources, supervision. Leila Naji: writing – review & editing. Mohammad Reza Ganjali: conceptualization.

Conflicts of interest

There are no conflicts to declare.

References

1 S. Y. Pan, A. Z. Haddad, A. Kumar and S. W. Wang, *Water Res.*, 2020, **183**, 116064.
2 M. Zong, Y. Zhang, K. Li, C. Lv, P. Tian, Y. Zhao and B. Liang, *Electrochim. Acta*, 2020, **329**, 135089.
3 R. Broséus, J. Cigana, B. Barbeau, C. Daines-Martinez and H. Suty, *Desalination*, 2009, **249**(1), 217–223.
4 M. A. Anderson, A. L. Cudero and J. Palma, *Electrochim. Acta*, 2010, **55**(12), 3845–3856.
5 Q. Jiang, Y. Han, W. Tang, H. Zhu, C. Gao, S. Chen and Z. L. Wang, *Nano Energy*, 2015, **15**, 266–274.
6 G. Divyapriya, K. K. Vijayakumar and I. Nambi, *Desalination*, 2019, **451**, 102–110.
7 A. Hassanvand, PhD thesis, Universuty of Melbourne, 2018.
8 K. Tang, Y. H. Kim, J. Chang, R. T. Mayes, J. Gabitto, S. Yiacoumi and C. Tsouris, *Chem. Eng. J.*, 2019, **357**, 103–111.
9 M. R. Vengatesan, I. F. F. Darawsheh, B. Govindan, E. Alhseinat and F. Banat, *Electrochim. Acta*, 2019, **297**, 1052–1062.
10 S. Kim, J. Lee, C. Kim and J. Yoon, *Electrochim. Acta*, 2016, **203**, 265–271.
11 J. Oladunni, J. H. Zain, A. Hai, F. Banat, G. Bharath and E. Alhseinat, *Sep. Purif. Technol.*, 2018, **207**, 291–320.
12 W. Tang, J. Liang, D. He, J. Gong, L. Tang, Z. Liu and G. Zeng, *Water Res.*, 2019, **150**, 225–251.
13 J. Ma, L. Wang and F. Yu, *Electrochim. Acta*, 2018, **263**, 40–46.
14 B. Senthilkumar, D. Meyrick, Y. S. Lee and R. K. Selvan, *RSC Adv.*, 2013, **3**(37), 16542–16548.
15 S. Porada, R. Zhao, A. Van Der Wal, V. Presser and P. M. Biesheuvel, *Prog. Mater. Sci.*, 2013, **58**(8), 1388–1442.
16 M. E. Suss, S. Porada, X. Sun, P. M. Biesheuvel, J. Yoon and V. Presser, *Energy Environ. Sci.*, 2015, **8**(8), 2296–2319.
17 J. Lee, S. Kim, C. Kim and J. Yoon, *Energy Environ. Sci.*, 2014, **7**(11), 3683–3689.
18 O. Barbieri, M. Hahn, A. Herzog and R. Kötz, *Carbon*, 2005, **43**(6), 1303–1310.
19 F. Zhou, T. Gao, M. Luo and H. Li, *Sep. Purif. Technol.*, 2018, **191**, 322–327.
20 C. Zhang, D. He, J. Ma, W. Tang and T. D. Waite, *Water Res.*, 2018, **128**, 314–330.
21 M. T. Z. Myint, S. H. Al-Harthi and J. Dutta, *Desalination*, 2014, **344**, 236–242.
22 C. Kim, J. Lee, S. Kim and J. Yoon, *Desalination*, 2014, **342**, 70–74.
23 A. G. El-Deen, J.-H. Choi, C. S. Kim, K. A. Khalil, A. A. Almajid and N. A. M. Barakat, *Desalination*, 2015, **361**, 53–64.
24 H. Yin, S. Zhao, J. Wan, H. Tang, L. Chang, L. He and Z. Tang, *Adv. Mater.*, 2018, **201325**(43), 6270–6276.
25 X. Gu, M. Hu, Z. Du, J. Huang and C. Wang, *Electrochim. Acta*, 2015, **182**, 183–191.
26 Y.-H. Liu, H.-C. Hsi, K.-C. Li and C.-H. Hou, *ACS Sustainable Chem. Eng.*, 2016, **4**(9), 4762–4770.
27 A. S. Yasin, M. Obaid, I. M. A. Mohamed, A. Yousef and N. A. M. Barakat, *RSC Adv.*, 2017, **7**(8), 4616–4626.
28 A. G. El-Deen, N. A. M. Barakat, K. A. Khalil, M. Motlak and H. Y. Kim, *Ceram. Int.*, 2014, **40**(9), 14627–14634.
29 D. Cai, D. Wang, C. Wang, B. Liu, L. Wang, Y. Liu and T. Wang, *Electrochim. Acta*, 2015, **151**, 35–41.
30 Y. Gao, S. Chen, D. Cao, G. Wang and J. Yin, *J. Power Sources*, 2010, **195**(6), 1757–1760.
31 J. Wang, X. Zhang, Q. Wei, H. Lv, Y. Tian, Z. Tong and L. Mai, *Nano Energy*, 2016, **19**, 222–233.
32 M. Kandasamy, S. Sahoo, S. K. Nayak, B. Chakraborty and C. S. Rout, *J. Mater. Chem. A*, 2021, **9**(33), 17643–17700.
33 S. Sahoo, K. Krishnamoorthy, P. Pazhamalai, V. K. Mariappan and S. J. Kim, *Inorg. Chem. Front.*, 2019, **6**(7), 1775–1784.
34 Z. Cao, Z. Yang, C. Zhang, L. Xie, X. Zhao, P. Pan and J. Zhao, *J. Mater. Sci.: Mater. Electron.*, 2020, **31**(3), 2406–2415.
35 S. Wang, S. Wang, G. Wang, X. Che, D. Li, C. Li and J. Qiu, *Mater. Today Commun.*, 2020, **23**, 100904.
36 D. Xie, S. Chen, Z. Zhang, J. Ren, L. Yao, L. Wu and X. Xu, *J. Power Sources*, 2018, **389**, 140–147.
37 S. Habibzadeh, A. Kazemi-Beydokhti, A. A. Khodadadi, Y. Mortazavi, S. Omanovic and M. Shariat-Niassar, *Chem. Eng. J.*, 2010, **156**(2), 471–478.
38 S. Habibzadeh, A. A. Khodadadi and Y. Mortazavi, *Sens. Actuators, B*, 2010, **144**(1), 131–138.
39 H. Fathi, S. M. Masoudpanah, S. Alamolhoda and H. Parnianfar, *Ceram. Int.*, 2017, **43**(10), 7448–7453.
40 S. K. Meher and G. R. Rao, *J. Phys. Chem. C*, 2011, **115**(31), 15646–15654.
41 P. Simon, Y. Gogotsi and B. Dunn, *Science*, 2014, **343**(6176), 1210–1211.
42 V. Augustyn, P. Simon and B. Dunn, *Energy Environ. Sci.*, 2014, **7**(5), 1597–1614.
43 J. Lang, X. Yan and Q. Xue, *J. Power Sources*, 2011, **196**(18), 7841–7846.
44 J. Xie, H. Cao, H. Jiang, Y. Chen, W. Shi, H. Zheng and Y. Huang, *Anal. Chim. Acta*, 2013, **796**, 92–100.
45 H. Younes, F. Ravaux, N. El Hadri and L. Zou, *Electrochim. Acta*, 2019, **306**, 1–8.
46 H. Chen, C. Xue, Z. Hai, D. Cui, M. Liu, Y. Li and W. Zhang, *J. Alloys Compd.*, 2020, **819**, 152939.
47 B. Babu, A. N. Kadam, R. Ravikumar and C. Byon, *J. Alloys Compd.*, 2017, **703**, 330–336.
48 Y. Qi and J. Zhang, *Composites, Part B*, 2019, **162**, 112–121.
49 H. Wang, Y. Fu, X. Wang, J. Gao, Y. Zhang and Q. Zhao, *J. Alloys Compd.*, 2015, **639**, 352–358.
50 A. N. Naveen and S. Selladurai, *RSC Adv.*, 2015, **5**(80), 65139–65152.

51 J. Yan, T. Wei, W. Qiao, B. Shao, Q. Zhao, L. Zhang and Z. Fan, *Electrochim. Acta*, 2010, **55**(23), 6973–6978.
52 W. Tong, Y. Wang, Y. Bian, A. Wang, N. Han and Y. Chen, *Nanoscale Res. Lett.*, 2020, **15**(1), 1–12.
53 S. Zhu, X. Yang, T. Li, F. Li and W. Cao, *J. Alloys Compd.*, 2017, **721**, 149–156.
54 Y. Chen, Y. Zhang and S. Fu, *Mater. Lett.*, 2007, **61**(3), 701–705.
55 X. Yang, Y. Wang, H. Xiong and Y. Xia, *Electrochim. Acta*, 2007, **53**(2), 752–757.
56 R. K. Sharma, H.-S. Oh, Y.-G. Shul and H. Kim, *Phys. B*, 2008, **403**(10–11), 1763–1769.
57 X. He, M. Yang, P. Ni, Y. Li and Z.-H. Liu, *Colloids Surf., A*, 2010, **363**(1–3), 64–70.
58 F. Manteghi, S. H. Kazemi, M. Peyvandipour and A. Asghari, *RSC Adv.*, 2015, **5**(93), 76458–76463.
59 Z. Tong, S. Liu, Y. Zhou, J. Zhao, Y. Wu, Y. Wang and Y. Li, *Energy Storage Mater.*, 2018, **13**, 223–232.
60 Q. Jiang, Y. Han, W. Tang, H. Zhu, C. Gao, S. Chen and Z. L. Wang, *Nano Energy*, 2015, **15**, 266–274.
61 M. R. Vengatesan, I. F. Fahmi Darawsheh, B. Govindan, E. Alhseinat and F. Banat, *Electrochim. Acta*, 2019, **297**, 1052–1062.
62 R. Fateminia, S. Rowshanzamir and F. Mehri, *Sep. Purif. Technol.*, 2021, **274**, 119108.
63 Y. Bouhadana, E. Avraham, M. Noked, M. Ben-Tzion, A. Soffer and D. Aurbach, *J. Phys. Chem. C*, 2011, **115**(33), 16567–16573.
64 Y. M. Volfkovich, *Russ. J. Electrochem.*, 2020, **56**(1), 18–51.
65 J. Lee and J. Choi, *J. Membr. Sci.*, 2012, **409–410**, 251–256.
66 Y. Ha, H. Lee, H. Yoon, D. Shin, W. Ahn, N. Cho and Y. Cho, *Sep. Purif. Technol.*, 2021, **254**, 117500.